

Direct measurement of the branching ratio Γ_n/Γ_f of ^{238}U in inelastic alpha scattering in the giant resonance region

P. J. Countryman,* K. A. Griffioen,[†] K. Van Bibber,[‡] and M. R. Yearian

Department of Physics and High Energy Physics Laboratory, Stanford University, Stanford, California 94305

J. R. Calarco

Department of Physics, University of New Hampshire, Durham, New Hampshire 03824

(Received 27 July 1989)

We have directly measured, for the first time, the neutron-fission branching ratio, Γ_n/Γ_f , of an actinide nucleus (^{238}U) excited in inelastic scattering as a function of excitation energy. This was accomplished using a $\approx 4\pi$ array of fission counters to separate fission neutrons from decay neutrons in the simultaneous coincidence experiments $(\alpha, \alpha'f)$ and $(\alpha, \alpha'n\bar{f})$. The measured branching ratio agrees well with previous photoneutron data. In a separate experiment, we have measured the angular distribution of alpha particles scattered from ^{238}U in coincidence with fission decay $(\alpha, \alpha'f)$. This provides us with an estimate of the cross section (in the fission channel) for exciting the isoscalar giant monopole and giant quadrupole resonances. This estimate, combined with the Γ_n/Γ_f measurement, allows us to place bounds on the neutron-fission branching ratio for the isoscalar giant monopole and giant quadrupole resonances themselves.

I. INTRODUCTION

Although many¹⁻⁶ have studied the decay of the isoscalar giant quadrupole (GQR) and monopole (GMR) resonances in ^{238}U , few have been able to agree on the strengths and branching ratios involved. Early $(\alpha, \alpha'f)$ measurements¹ seemed to indicate that the fission probability of the GQR is much less than that of the giant dipole resonance (GDR) in the same region of excitation energy [$P_f(E1) \approx 0.22$].^{7,8} By measuring both cross sections $\sigma(\alpha, \alpha'f)$ and $\sigma(\alpha, \alpha')$, one can directly obtain the fission probability $P_f = \Gamma_f/\Gamma_{\text{tot}}$. The presence of contaminant peaks in the (α, α') cross section, as well as a large continuum background, complicates the analysis of these data. Inclusive electron scattering measurements (e, e') of the giant resonances,⁹ on the other hand, are very difficult because of the presence of the radiative tail from elastic scattering. This tail disappears from the coincidence $(e, e'f)$ data, leaving virtually no background; however, the large uncertainties in the $(e, e'f)$ cross sections make the extraction of fission probabilities nearly impossible. Thus, conclusions about resonant fission probabilities from $(e, e'f)$ measurements must be made with reference to sum rules or strengths calculated for collective states, e.g., the quasiparticle random-phase approximation (QRPA).¹⁰ The three existing sets of $(e, e'f)$ cross sections⁴⁻⁶ agree in shape and magnitude, but the extracted $E2/E0$ strength functions differ significantly depending on whether one uses Tassie-model^{4,5} form factors in the analysis [resulting in $P_f(E2) \approx \frac{1}{3}P_f(E1)$ if the resonance exhausts the sum rule] or whether one attempts to deduce the form factors from the data [yielding $P_f(E2) \approx P_f(E1)$].⁶ The latter analysis, however, yields an $E1$ transition radius much greater than that predicted by the QRPA (Ref. 10) or the

Deal-Fallieros-Noble sum rule.¹¹

Given that exclusive experiments eliminate many sources of background from the spectra, perhaps the cleanest way to measure a fission probability is by observing all possible decay channels. In the case of the actinides, fission and neutron emission overwhelmingly dominate all other open channels. Hence, by measuring the ratio of decay widths Γ_n/Γ_f we can effectively determine P_f . Such a simultaneous measurement eliminates many systematic errors involved in the comparisons with inclusive data. Moreover, the neutron energy spectra may reveal nonstatistical components of the decay. The challenge of such an experiment, however, lies in the separation of post-fission neutrons (having multiplicities $\bar{\nu} \approx 2.5-4$) from primary neutrons. We have overcome this problem by developing an efficient veto for fission events. Our measurement is the first of its kind and demonstrates the feasibility of measuring primary neutron spectra in fissionable nuclei. The expression $(\alpha, \alpha'n\bar{f})$ denotes the primary neutron measurements by indicating the fission veto.

II. EXPERIMENTAL SETUP

The setup for this experiment is shown in Fig. 1. Six parallel-plate avalanche counters (PPAC's) surround the target, three in the front hemisphere and three in the back. Three solid-state detector telescopes view the target through the interstices of the PPAC array, at an angle of 17.0° with respect to the beam direction. Eight neutron time-of-flight counters were placed in the back hemisphere. A beam of 120 MeV alpha particles was supplied by the 88-Inch Cyclotron. Coincidences between any solid-state telescope and any neutron or fission counter were recorded.

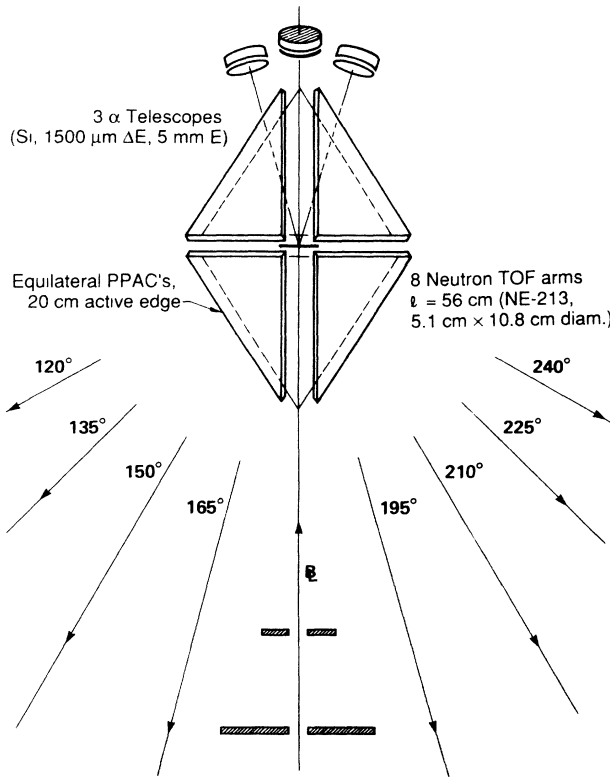


FIG. 1. Diagram of experimental setup. 120 MeV α -particle beam is incident from bottom of figure. Arrows indicate angles of neutron counters. Beam passes through two carbon collimators before striking target.

A. The beam and target

The beam current was always kept below 10 nA, and normally was about 5 nA. To keep the neutron background low, the beam was stopped 4.3 m from the target in a Faraday cup, which was surrounded by borated paraffin and concrete blocks. The current in the Faraday cup was integrated for each data-taking run. Scalers counted the number of valid coincidence events, and also the number of events accepted by the computer. The ratio of these numbers allowed us to correct for computer dead time.

The target was self-supporting depleted uranium (565 $\mu\text{g}/\text{cm}^2$). The target was stored in a vacuum, and the scattering chamber was filled with argon before the target was mounted in the chamber. This was done in order to reduce oxidation of the target.

B. Parallel plate avalanche counters

Parallel-plate avalanche counters are known to be highly efficient at detecting fission fragments, and provide good separation of the fission signals from noise.¹² The PPAC's were in the shape of equilateral triangles measuring 23.5 cm on the outer edge of the frame, whose width represented a dead strip around the perimeter of 0.95 cm. The total active area of each counter was 177 cm^2 . The PPAC's formed the faces of a hexahedron, centered on

TABLE I. Parallel-plate avalanche counter solid angles. Statistical error in solid angle is ± 15 msr in each counter. Angular position of center of each PPAC is also given.

PPAC	$\langle \theta \rangle$	$\langle \phi \rangle$	$\Delta\Omega/2\pi$	$\Delta\Omega$ (msr)
1	33	180	0.128	807
2	33	-60	0.125	783
3	38	60	0.159	998
4	141	180	0.127	797
5	129	-60	0.229	1437
6	129	60	0.223	1403

the target position. A space of ≈ 4 cm between the edges of the PPAC's permitted the beam to enter and exit the detector array. It also left sufficient space for the three solid-state detector telescopes to view the target. The solid angle subtended by each PPAC is given in Table I. A Monte Carlo calculation showed that, for binary fission fragments emitted isotropically, there was a 77% probability that at least one fragment would strike the active area of a PPAC. The missing solid angle was largely around $\theta=90^\circ$, i.e., in the plane of the target.

The actual probability to detect a fragment was slightly smaller; $67\pm 5\%$. This was primarily due to degradation of the pulse height of fission signals during the course of the experiment, which caused as many as 10% of the fission fragments to fall below the hardware threshold. [The probability to detect a fragment was determined by requiring that the measured cross section $\sigma(\alpha, \alpha' n \bar{f})$ vanish when the neutron energy exceeds the kinematic limit, $E_n > E_\alpha - E'_\alpha - S_n$, where S_n ($=6.15$ MeV) is the neutron separation energy of ^{238}U .] A typical pulse-height spectrum from one of the PPAC's is shown in Fig. 2.

C. ΔE -E telescopes

Three solid-state ΔE -E telescopes viewed the target through the space between the forward PPAC's. These made an angle of 17° with the beam, a local maximum in the $L=0$ and $L=2$ angular distributions. The distance from the target to the collimators was 24.5 cm. The tantalum collimators on each telescope had an area of 0.39 cm^2 each, and the solid angle subtended by each telescope was 0.65 msr.

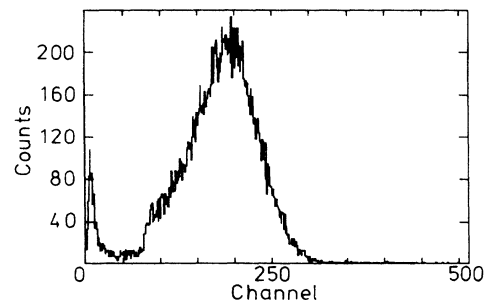


FIG. 2. Representative pulse-height spectrum from parallel-plate avalanche counter.

Each telescope consisted of two solid-state detectors, a thin (1.5 mm) ΔE and a thick (5 mm) Si(Li) E detector. Each had a resolution of 100–200 keV for 120 MeV alpha particles. We could easily identify alpha particles that entered the E detector ($E'_\alpha \geq 60$ MeV).

D. Neutron counters

Eight neutron time-of-flight arms were placed in the backward hemisphere, 56.5 cm from the target position. The active volume of each counter (5.1 cm \times 11.4 cm diam) was filled with NE-213 liquid scintillator. The scintillator wells were coupled via clear plastic light guides to photomultiplier tubes (PMT's). Four of the counters used 2-inch PMT's (RCA 8575) and four used 5-inch tubes (RCA 4522).

The time spectrum between the alpha telescopes and the neutron detectors is shown in Fig. 3. The large sharp peak is due to the true alpha-gamma coincidences, and the broad peak immediately to the right is due to the true alpha-neutron coincidences. The smaller peaks are the random gamma coincidences, spaced by the cyclotron beam period of 83 ns.

A two-dimensional plot of E_α vs τ (time of flight) is shown in Fig. 4. Note that the band of true neutrons lies above the kinematic limit (solid line) at $E_x \geq S_n$. (Since $d\Omega_f < 4\pi$, there are fission neutrons that must still be subtracted from the kinematically forbidden region.)

1. Digital pulse-shape discrimination

Since n and γ counting rates for our unshielded neutron detectors were nearly equal, it was important to have as high a rejection factor for gammas as possible. Gamma rejection was performed off line using digital pulse-shape discrimination. The signal from the anode of the photomultiplier tube is integrated in two charge-sensitive analog-to-digital converters (ADC's). One ADC integrates over the entire anode signal (≈ 100 ns) and the

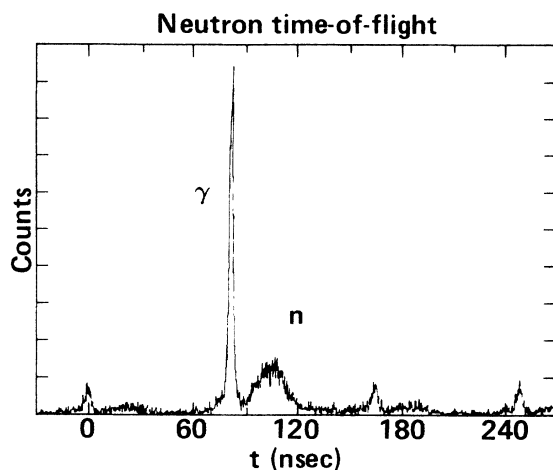


FIG. 3. Time difference spectrum between α telescope and neutron counters, before pulse-shape discrimination is applied. Cyclotron beam burst period is 83 ns.

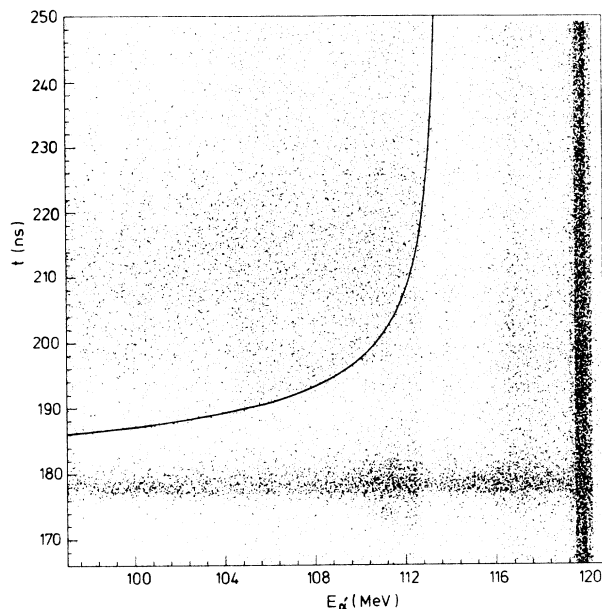


FIG. 4. Energy of scattered α particle (E_α) vs neutron time of flight (τ). Curve indicates kinematic limit for neutrons from the $(\alpha, \alpha' n \bar{f})$ channel. Horizontal line at ≈ 178 ns is due to prompt gammas. Vertical line at 120 MeV is due to (random) elastics. Neutron threshold occurs at $E_\alpha \approx 114$ MeV.

other over the rising edge of the signal (≈ 5 ns). A scatter plot of the digitized signal shows two bands, one for neutrons and one for gamma rays (Fig. 5). Appropriate software cuts can then be made to exclude the gammas. By applying cuts on time of flight and pulse shape, we were able to reject 98% of the gammas.

2. Neutron efficiency measurement

The neutron efficiency was measured by placing a ^{252}Cf source at the target position. The source was sealed in a proportional counter that took the place of the solid-state telescopes in the logic electronics. Neutron-fission coincidences were recorded, with time-of-flight (and thus neu-

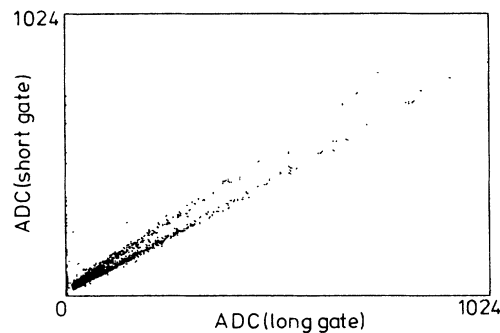


FIG. 5. Scatter plot showing digital pulse-shape discrimination. Horizontal axis is area of entire pulse, vertical axis is area in leading edge. Upper diagonal line identified as gammas, lower diagonal line as neutrons.

TABLE II. α -telescope angles and solid angles for the $(\alpha, \alpha'f)$ experiments. Uncertainty in solid angles is $\pm 4\%$, uncertainty in angles is $\pm 0.2^\circ$. Right-hand side column shows the integrated charge in the Faraday cup (uncertain by $\pm 5\%$) for the two sets of angles.

Telescope No.	1	2	3	4	Charge (μC)
$\Delta\Omega$ (msr)	0.26	0.31	0.39	0.48	
θ'_α (1)	7.3°	11.1°	14.8°	18.9°	2528
θ'_α (2)		13.2°	17.2°	21.2°	586

tron energy) and pulse-shape discrimination information included. The spectrum of neutrons from the spontaneous fission of ^{252}Cf is well known,¹³ and may be approximated as a Maxwellian energy spectrum:

$$N(E_n)dE_n = \text{const} \times \sqrt{E/T} \exp(-E/T), \quad (1)$$

with $T=1.42$ MeV and multiplicity $\bar{\nu}=3.76$ per fission. Dividing the measured spectrum by the theoretical spectrum gave us the solid angle efficiency product of the neutron counters as a function of neutron energy from 0.5 to 6 MeV. We also calculated the efficiency using the formalism of Drosog.¹⁴ The calculation matched the measured efficiency well, and was used to extrapolate the solid angle efficiency function to energies above 6 MeV.

E. Logic

We defined a coincidence event by a signal in one of the solid-state counters and a simultaneous signal in either a PPAC (αf) or a neutron counter (αn). For each coincidence event we recorded the energy deposited in the ΔE and E counters, the energy signals in the PPAC's and neutron counters, the time difference between the firing of the ΔE counter and the PPAC's and neutron counters, and a bit pattern that recorded which counters fired. This was enough information to permit us to separate detected neutrons as primary or post-fission decays, up to a small correction because of the PPAC's solid angle efficiency product being less than 4π . Identification of α particles and neutron-gamma discrimination was done off line.

F. $(\alpha, \alpha'f)$ experiment

In a separate experiment, we measured the angular distribution of alpha particles in coincidence with fission fragments, this time using four ΔE - E telescopes on a movable arm, and the backward hemisphere of the PPAC's array. The beam energy was 120 MeV, as in the neutron experiment. Because we did not have to worry about high rates in the neutron counters, we ran at a beam current of 25 nA. The solid angles of the alpha telescopes are listed in Table II. The time spectrum for coincidences between the alpha telescopes and the PPAC's is shown in Fig. 6.

III. DATA REDUCTION

On the first pass through the data, events were rejected for which two solid-state telescopes fired simultaneously

($\sim 0.1\%$) and events that did not satisfy the alpha-particle identification. For each event, it was determined how many PPAC's fired above threshold and which neutron counters passed the pulse-shape discrimination cut. The time-of-flight information was corrected for the different time delays of each neutron counter so that the time spectrum could be summed over all the neutron counters. Each fission event was classified according to the time peak in which it occurred (true, first random, second random, etc.)

On the second pass through the data, the energy of the scattered alpha particles was calculated from the ΔE and E signals. One-dimensional spectra of scattered alpha-particle energy for the $(\alpha, \alpha'f)$ events were formed, gated according to the fission time peak (true or random). After subtracting the randoms from the trues, the data from the three telescopes were summed. The $(\alpha, \alpha'f)$ spectrum was normalized to an absolute cross section, using the nominal target thickness, integrated charge (from the Faraday cup), the solid angles of the alpha telescopes, and the measured efficiency of the PPAC array. This quantity is plotted in Fig. 7(a).

The neutron-coincident events $(\alpha, \alpha'n)$ were sorted into four two-dimensional spectra of alpha-particle energy versus time of flight, gated according to the timing of the fission signal (true, first random, second random, or no fission). The two-dimensional spectra were split according to the timing of the neutron signal (random or true), and the appropriate random corrections were made to produce spectra of $(\alpha, \alpha'n\bar{f})$ and $(\alpha, \alpha'n\bar{f})$. These spectra were then corrected for the overall efficiency, ϵ , of the PPAC array, ϵ :

$$N_1(\alpha, \alpha'n\bar{f}) = N_0(\alpha, \alpha'n\bar{f}) - \frac{1-\epsilon}{\epsilon} N_0(\alpha, \alpha'nf), \quad (2a)$$

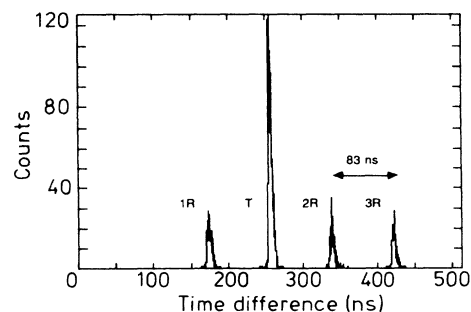


FIG. 6. Time difference spectrum between α telescopes and PPAC's. The large peak contains the true coincidences, the smaller peaks are randoms.

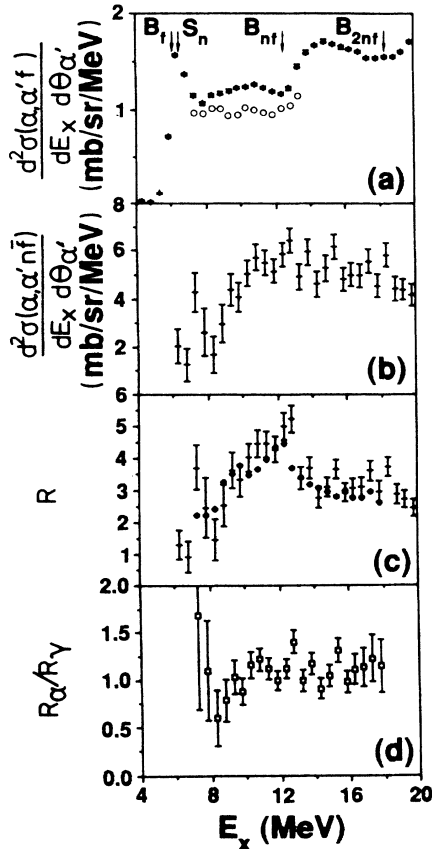


FIG. 7. The spectra $(\alpha, \alpha' f)$ (a), and $(\alpha, \alpha' n \bar{f})$ (b), at $\theta_{\alpha'} = 17^\circ$. Open symbols in (a) are the background derived from the fitting procedure described in the text. (c) The ratios R_α (this work) and R_γ (Ref. 7). (d) The ratio R_α/R_γ .

$$N_1(\alpha, \alpha' n f) = \frac{1}{\epsilon} N_0(\alpha, \alpha' n f). \quad (2b)$$

(N_0 refers to the coincidence spectra corrected for accidental coincidences, but not corrected for the less-than-perfect efficiency of the fission counters. N_1 refers to the fully corrected coincidence spectra.) Note that this expression manifestly conserves the total number of true neutron coincidences:

$$\begin{aligned} N_1(\alpha, \alpha' n \bar{f}) + N_1(\alpha, \alpha' n f) \\ = N_0(\alpha, \alpha' n \bar{f}) + N_0(\alpha, \alpha' n f). \end{aligned} \quad (3)$$

We divided the two-dimensional spectrum of $(\alpha, \alpha' n \bar{f})$ events by the neutron efficiency and solid angle. Assuming the neutron energy spectra were Maxwellian, we estimated the number of events cut off by the energy threshold of 0.5 MeV for each value of the scattered alpha energy. Finally, we summed over the neutron energy to obtain the cross section

$$d^2\sigma(\alpha, \alpha' n \bar{f})/dE'_\alpha d\Omega'_\alpha$$

as a function of excitation energy. This cross section is plotted in Fig. 7(b).

IV. CROSS SECTIONS

A. $(\alpha, \alpha' f)$, $(\alpha, \alpha' n \bar{f})$ at 17°

Figure 7 presents an overview of the data. The $(\alpha, \alpha' f)$ spectrum of Fig. 7(a) (which, by the nature of our PPAC array, is automatically integrated over fission-fragment solid angle), displays a sharp rise at fission threshold (5.9 MeV) followed by a steep drop when the neutron channel begins to compete ($S_n = 6.15$ MeV). The isoscalar giant quadrupole resonance sits near $E_x = 10$ MeV and appears to have a bimodal structure. Second- and third-chance fission cause the increase in cross section at 12 and 18 MeV, respectively. The isoscalar giant monopole resonance at $E_x \approx 13$ MeV is hard to see because of the rapidly changing fission probability in this region. The neutron spectrum $(\alpha, \alpha' n \bar{f})$ of Fig. 7(b) shows a structureless, slow increase above threshold, and a gradual falloff after the onset of second-chance fission. The statistics here are quite poor since the efficiency for neutron detection is very low. Figure 7(c) shows the ratio of Figs. 7(a) and (b), $R_\alpha \equiv (\alpha, \alpha' n \bar{f})/(\alpha, \alpha' f)$ (crosses) and the equivalent quantity R_γ for the Saclay real-photon data (solid points). The agreement in shape and magnitude is excellent. Our cross sections $\sigma(\alpha, \alpha' n \bar{f})$ are actually a weighted sum over the neutron decay channels,

$$\sigma(\alpha, \alpha' n \bar{f}) = \sigma(n) + 2\sigma(2n) + 3\sigma(3n) + \dots \quad (4)$$

In order to make the comparison with the photon data, we have formed the ratio

$$R_\gamma = [\sigma(\gamma, n) + 2\sigma(\gamma, 2n) + \dots] / \sigma(\gamma, f)$$

(Ref. 15). Figure 7(d) gives the ratio R_α/R_γ , which is unity within statistical errors. This indicates that the summed contribution of resonance and continuum background in α scattering has the same branching ratio as the giant dipole resonance (GDR) to within our 15% experimental accuracy.

B. $(\alpha, \alpha' f)$ angular distribution

Figure 8 shows typical spectra from the high-statistics $^{238}\text{U}(\alpha, \alpha' f)$ experiment. The spectra shown were measured at $\theta_{\alpha'} \approx 13.2^\circ$ [Fig. 8(a)], 14.8° [Fig. 8(b)], and 17.2° [Fig. 8(c)]. Since we did not take neutron data in this experiment, we were unable to use the kinematic limit for neutron emission to check the efficiency of the PPAC array. We therefore matched the cross section at 17.2° to the cross section measured in the $(\alpha, \alpha' n \bar{f})$ experiment at 17° . This implied a PPAC efficiency of 56% for this run, compared to the Monte Carlo result of 63%. This is roughly consistent with the ratio of measured efficiency to geometric efficiency (67%/77%) from the $(\alpha, \alpha' n \bar{f})$ experiment.

C. Estimate of resonant cross section

Assuming that the branching ratio for the background alone equals that of the dipole resonance, we can place limits on Γ_n/Γ_f for the GQR and the GMR. To do so we need to know the resonant and background contribu-

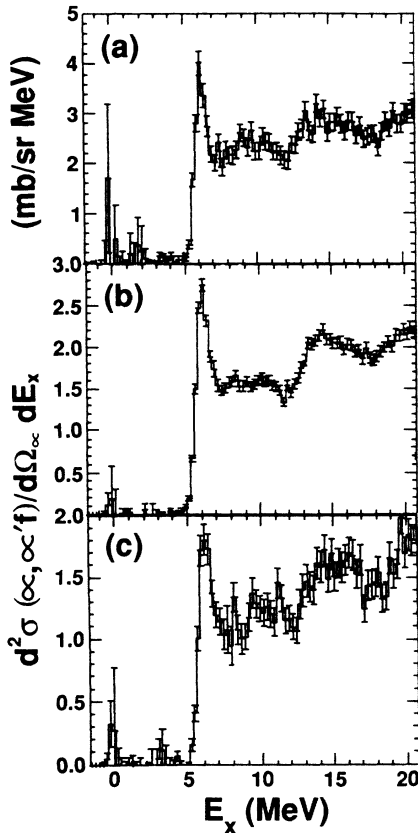


FIG. 8. Measured cross sections $d^2\sigma(\alpha, \alpha'f)/d\Omega dE_x$ from a dedicated $(\alpha, \alpha'f)$ experiment. Shown here are data taken at $\theta_{\alpha'}=13.2^\circ$ (a), 14.8° (b), and 17.2° (c).

tions to $(\alpha, \alpha'f)$. We have fit these angular distributions to the form

$$\sigma(\alpha, \alpha'n\bar{f}) = A(E_x)e^{-\theta/\theta_0} + \frac{dB}{dE_x}P_f F(E_x, \theta), \quad (5)$$

in which $\theta_0 = aE_x + b$, E_x is the excitation energy, and θ is the α scattering angle. The first term describes the featureless background beneath the resonance, which has an exponential distribution that depends on E_x and the fitting parameters a and b . The second term is the resonant cross section expressed as a differential strength $(dB/dE_x)P_f$ in the fission channel multiplied by the cross section per unit strength $F(E_x, \theta)$ taken from a distorted-wave calculation.

We have calculated $F(E_x, \theta)$ for $E0$ and $E2$ with the computer codes DWUCK (Ref. 16) and ECIS (Ref. 17), respectively, following Brandenburg *et al.*³ (see Table III)

TABLE III. Optical-model parameters used in DWBA and ECIS calculations. These parameters are the same as those used in the DWBA calculation of Ref. 3. $U(r) = V(r) + iW(r)$, V and W are Woods-Saxon potentials with radius parameters $r_{R,I}$ and thickness parameters $a_{R,I}$. A Coulomb potential for a uniform spherical charge distribution of radius $r_C A^{1/3}$ was added to $U(r)$.

V	-155 MeV	W	-23.26 MeV		
r_R	1.282 fm	r_I	1.478 fm	r_C	1.4 fm
a_R	0.677 fm	a_I	0.733 fm		

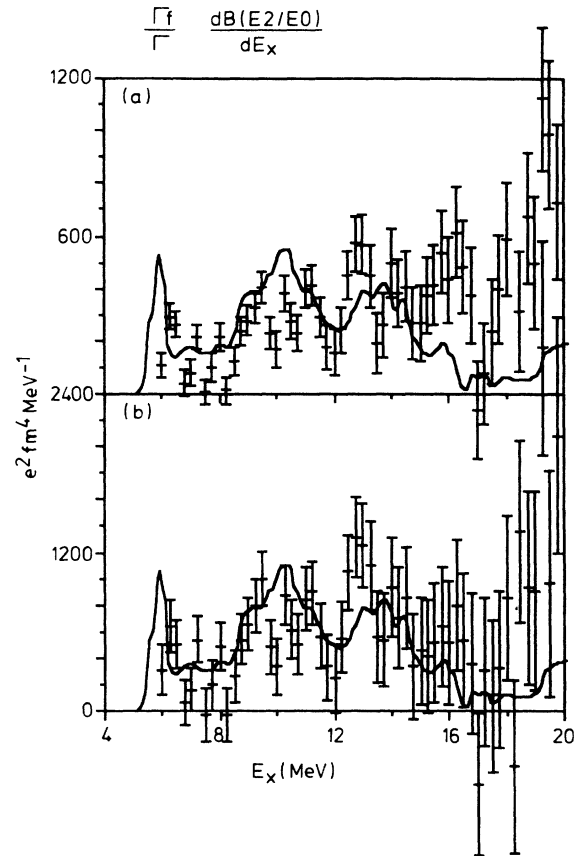


FIG. 9. The $E2/E0$ strength found in $(\alpha, \alpha'f)$, assuming the strength is (a) entirely $E2$; (b) entirely $E0$. In both panels, the solid line is the corresponding strength function from the $(e, e'f)$ work of Ref. 6.

by scaling up the optical-model radii measured for ^{208}Pb to those appropriate for ^{238}U . At the angles greater than 7° , the $E2$ and $E0$ angular distributions are in phase and differ from each other only in the relative depth of the minima. As a consequence, we cannot separate these two strengths. Rather, we have analyzed the full range of excitation energy using either the $E2$ or $E0$ calculated angular distributions. The $(\alpha, \alpha'f)$ data of Fig. 8 are well described by the fit. Figures 9(a) and (b) display the extracted multipole strength assuming $E0$ and $E2$ angular distributions, respectively. The differences in the resonant cross section in these two cases are slight. (The extracted strength, measured in units of $e^2 \text{fm}^4$, differs by a factor of 2 depending upon whether one assumes the strength to be $E0$ or $E2$.) Superimposed on both is the $E2/E0$ strength distribution derived from the most recent $(e, e'f)$ data.⁶

TABLE IV. Comparison of the $E2/E0$ strength (percentage of one isoscalar energy-weighted sum rule) found in $(\alpha, \alpha'f)$ (this work) and $(e, e'f)$ in Refs. 4–6. Numbers in parentheses result from assuming $(\Gamma_n/\Gamma_f)_\lambda = (\Gamma_n/\Gamma_f)_{E1}$. For this work, only statistical errors are shown.

Reference	E_x (MeV)	$E1$	$E0$	$E2$
$(e, e'f)$ (Ref. 4)	5.7–7.0			3.7 (8)
	7.0–11.7			10 (45)
$(e, e'f)$ (Ref. 5)	< 6.5			1.0 ± 0.4 (1.5 ± 0.6)
	< 11			7.9 ± 1.2 (33 ± 5.0)
	< 17.5	(80 ± 4)	32 ± 5 (102 ± 16)	
$(e, e'f)$ (Ref. 6)	< 6.5			2.0 ± 0.2 (3.8 ± 0.7)
	8–12			15 ± 1 (69 ± 5)
	< 12			19 ± 2 (80 ± 6)
	12–16.4		32 ± 3 (100 ± 9)	
	< 17.5	24 ± 1 (81 ± 4)		
This work	8–12			13.3 ± 1 (56 ± 5)
	12–16		50 ± 7 (156 ± 22)	

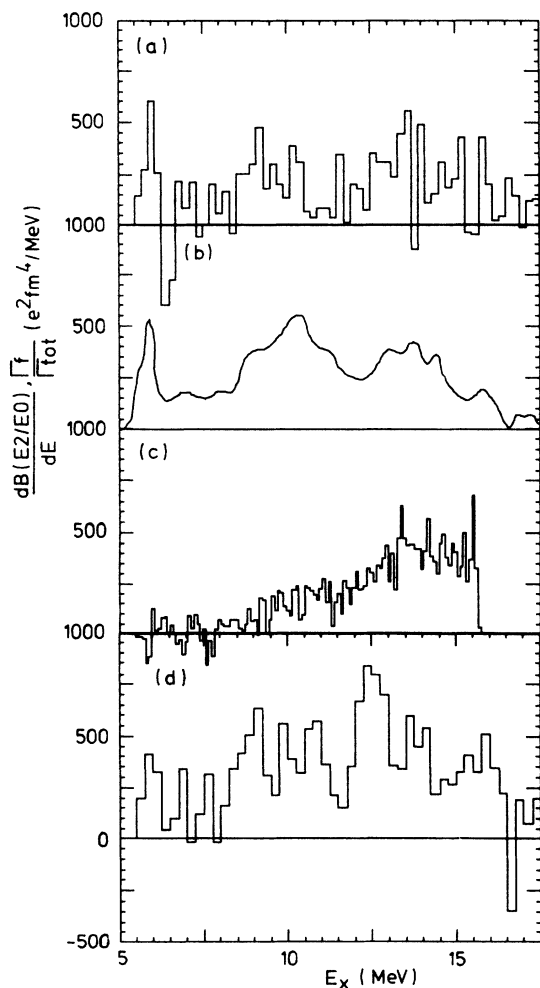


FIG. 10. Isoscalar giant quadrupole and giant monopole resonance strength in Refs. 5, 6, and 3 and the present work. (a) $dB(E2/E0)/dE_x$ from $^{238}\text{U}(e, e'f)$, Ref. 5. (b) Same as Ref. 6. (c) $dB(E0)/dE_x$ from $^{238}\text{U}(\alpha, \alpha'f)$, Ref. 3. (d) $dB(E2/E0)/dE_x$ from this work [same as Fig. 9(b)]. Except for (c), all are normalized assuming the strength is entirely $E2$.

One working hypothesis is to identify the broad bumps at 10 and 13 MeV with the GQR and GMR, respectively, as has been done in two recent coincident electron scattering experiments (Refs. 5 and 6). Under this assumption, one expects good agreement with the $(e, e'f)$ data around 10 MeV for the case in which the $L=2$ angular distribution was used to fit the $(\alpha, \alpha'f)$ data [Fig. 9(a)]. Similarly, the agreement with the $(e, e'f)$ data is expected to be better near 13 MeV when the $L=0$ angular distribution is used to fit the $(\alpha, \alpha'f)$ data [Fig. 9(b)]. In this case, the agreement with other experiments is quite good (see Table IV). Figure 10 shows the isoscalar $E2/E0$ strength found in two $(e, e'f)$ experiments,^{5,6} the $E0$ strength from Ref. 3, and the $E2/E0$ strength from this experiment.

With the resonant $(\alpha, \alpha'f)$ cross section in hand, we can now estimate the background contribution at 17° for both fission and neutron channels,

$$\sigma_{\text{BG}}(\alpha, \alpha'f) = \sigma(\alpha, \alpha'f) - \sigma_{\text{res}}(\alpha, \alpha'f) \quad (6)$$

and

$$\sigma_{\text{BG}}(\alpha, \alpha'n\bar{f}) = \sigma(\alpha, \alpha'n\bar{f}) - R_{\text{res}} \sigma_{\text{res}}(\alpha, \alpha'n\bar{f}), \quad (7)$$

in which R_{res} is the ratio

$$\sigma_{\text{res}}(\alpha, \alpha'n\bar{f}) / \sigma_{\text{res}}(\alpha, \alpha'f).$$

We can solve for R_{res} assuming that

$$R_{\text{BG}} \equiv \sigma_{\text{BG}}(\alpha, \alpha'n\bar{f}) / \sigma_{\text{BG}}(\alpha, \alpha'f) = R_\gamma.$$

We have done this twice, once taking R_γ from the data of Ref. 7, and once from Ref. 8. In this way we can see the sensitivity of R_{res} to uncertainty in R_{BG} .

The results averaged over each resonance are listed in Table V. Clearly, within the errors of the experiment the resonant contributions agree with the photon data. Unfortunately, the error bars are quite large. Systematic errors result from uncertainties in the PPAC's solid angle efficiency product ($\pm 5\%$), relative normalizations of $(\alpha, \alpha'f)$ data taken in separate runs ($\pm 5\%$), and the differences in R_γ taken from the two photoneutron ex-

TABLE V. Comparison of the neutron-fission yield ratio R for the isoscalar giant quadrupole and giant monopole resonances measured in this work, and the same quantities inferred from Refs. 1–6, averaged over the excitation energy of the isoscalar giant quadrupole resonance (≈ 8 –12 MeV) and the isoscalar giant monopole resonance (≈ 12 –16 MeV). For this work, two sets of values are shown, one for R_{BG} taken from the data of Ref. 7, and one R_{BG} from Ref. 8. The first error value shown is statistical, and the second is systematic. For the experiments that did not measure the neutron decay branch, the ratio R was formed by averaging the quantity $\bar{\nu}(E) \times (1 - P_f) / P_f$ over the indicated energy ranges, where $\bar{\nu}(E) = \sum_{\nu} \nu \sigma(\gamma, \nu n) / \sum_{\nu} \sigma(\gamma, \nu n)$, is taken from the data of Ref. 7, and P_f is the fraction and the energy-weighted sum rule observed in the fission decay channel. Also shown is R for the GDR obtained from Refs. 7 and 8.

Reference	E_x (MeV)	$E0$	$E2$
(γ, n) (Ref. 7)	8–12		3.6
	12–16	3.5	(E1 only)
(γ, n) (Ref. 8)	8–12	(E1 only)	3.6
	12–16	3.8	
$(\alpha, \alpha'f)$ (Ref. 1)	~ 8 –13		> 7
$(\alpha, \alpha'f)$ (Ref. 2)	~ 9 –12		3.1^{+2}_{-1}
$(\alpha, \alpha'f)$ (Ref. 3)	8–16	3.6^{+1}_{-1}	
$(e, e'f)$ (Ref. 4)	7–11.7		~ 9
$(e, e'f)$ (Ref. 5)	7–11		12 ± 2
	11–17.5	3.4 ± 1	
$(e, e'f)$ (Ref. 6)	8–12		4.4 ± 0.6
	12–16.4	3.4 ± 0.5	
This work			
(Ref. 7)	8–12		$3.4 \pm 1.1 \pm 3$
	12–16	$5.7 \pm 1.5 \pm 5$	
(Ref. 8)	8–12		$3.1 \pm 1.1 \pm 3$
	12–16	$3.1 \pm 1.5 \pm 5$	

periments ($\approx 8\%$). Because the GQR sits below the threshold for two-neutron emission, R_{res} is simply Γ_n / Γ_f , and is consistent with a normal (i.e., E1) fission probability. Adding all errors in quadrature gives a lower limit to the fission probability of one-half normal. That is consistent with the upper limit on the fission probability given in Ref. 1. Because the GMR sits between first- and second-chance fission plateaus, both R_{BG} and R_{res} are changing rapidly over the energy range of the monopole. Therefore, the average R_{res} for the monopole is quite sensitive to the competition between single and double neutron emission. The average neutron decay yield, $(\sigma_n + 2\sigma_{2n}) / \sigma_{\text{tot}}$, from Refs. 7 and 8 differ by 8% between 12 and 16 MeV, leading to very different values of R_{res} . If the cross section $\sigma_{\text{res}}(\alpha, \alpha'f)$ in this region is really due entirely to $L=0$ strength, it is doubtful that R_{res} could really be as large as is found by taking R_γ from Ref. 7. Taking $R_{\text{BG}} = R_\gamma$ from Ref. 8, we find that $R_{\text{res}} = R_\gamma$ within our statistical errors. Table V compares the ratios Γ_n / Γ_f for various experiments, assuming $\Gamma = \Gamma_n + \Gamma_f$.

D. Neutron energy spectrum

If the quadrupole fission probability were smaller than normal, it might be possible that the GQR would have a strong nonequilibrium decay component. If this is so, it could show up in the neutron energy spectra. (One such spectrum, integrated over $E_x = 8$ –12 MeV, is shown in

Fig. 11.) We formed the neutron energy spectra for all excitation energies from 6 to 23 MeV in 1 MeV steps, and fit each spectrum to a Maxwellian energy distribution, folded with the response function for the detectors. In all cases, the temperature parameter is consistent with a Fermi gas with level-density parameter $a = A/10$. (Similar fits to the fission-coincident neutron energy spectra yielded a temperature parameter of 1.0 ± 0.1 MeV, indepen-

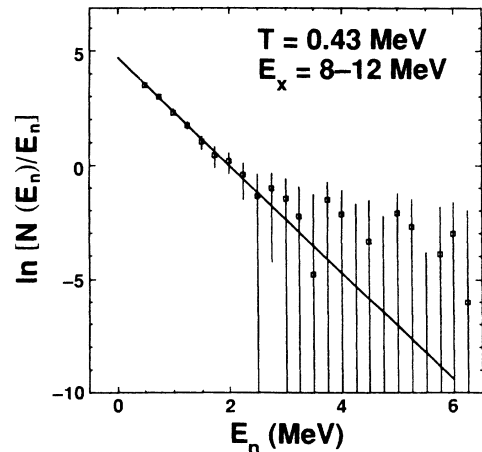


FIG. 11. Neutron energy spectrum from $^{238}\text{U}(\alpha, \alpha'nf)$, summed over $E_x = 8$ –12 MeV. Straight line indicates best-fit Maxwellian, with temperature parameter $T = 0.43$ MeV.

dent of excitation energy.) No significant peak in the spectrum occurs at large neutron energies, indicating that nonequilibrium decay is not significant. The low nonstatistical contribution is consistent with measurements of 10–15% on ^{208}Pb .¹⁸ Although the neutron counting statistics were rather poor, our experiment demonstrates the feasibility of measuring primary neutron spectra from fissionable nuclei.

V. CONCLUSIONS

We first reiterate the aforementioned (plausible) assumption (and made elsewhere^{5,6}) that the $E2/E0$ strength function should be divided at 12 MeV, with $E_x < 12$ MeV being assigned almost entirely to $E2$ and $E_x > 12$ MeV to $E0$ (see Fig. 10). Then our results ($\Gamma_n/\Gamma_f = 3-3.5$) are consistent with a normal fission probability for the GQR and exclude $P_f(E2) < \frac{1}{2}P_f(E1)$, the upper limit found in Ref. 1. The apparent lack of nonstatistical neutron decay is consistent with the conclusion of a normal fission probability. From the above value of Γ_n/Γ_f and our $(\alpha, \alpha'f)$ measurements, we conclude that the state at 10 MeV exhausts a large fraction of the isoscalar $E2$ sum rule (our data prefer a value of 70%).

But an alternative point of view is possible. Theory predicts mixing of the isoscalar giant quadrupole and giant monopole resonances in deformed nuclei. Indeed, the data of Brandenburg *et al.*³ [see Fig. 10(c)] show the presence of monopole strength in ^{238}U in two bumps: a large one at 13 MeV and a smaller bump at 10 MeV. If we subtract the $E0$ strength from Brandenburg's data from the $E2/E0$ strength from our $(\alpha, \alpha'f)$ angular distribution, and divide the resulting spectrum by the $E1$ fission probability, we can account for 50% of the isoscalar $E2$ energy weighted sum rule between 6 and 12 MeV, and another 50% between 12 and 16 MeV. While such a large shift in the location of the $E2$ strength is not predicted by theory, it would account for the apparent deficiency in $E2$ strength reported in Ref. 5. However, the *ad hoc* way in which we have extracted the multipole strength from our $(\alpha, \alpha'f)$ data makes it very uncertain that this analysis is quantitatively correct. We mainly wish to point out that the mixing of the isoscalar giant monopole and giant quadrupole resonance may be larger than is generally assumed.

In light of the uncertainties in making multipole assignments and deriving strength functions based on inelastic hadron scattering, our extracted branching ratios have large error bars. However, in view of the demonstrated quality of strength extractions from coincidence electron scattering, we venture that $(e, e'n\bar{f})$ measurements¹⁹ would provide more rigorous and direct bounds on Γ_n/Γ_f .

ACKNOWLEDGMENTS

We would like to thank R. G. Stokstad, C. Lyneis, and the staff of the LBL 88-Inch Cyclotron for reliable operations during the experiment. We would also like to thank A. Vèysiere for providing tables of photoneutron cross sections, and S. Brandenburg and M. N. Harakeh for as-

sistance with distorted-wave Born approximation (DWBA) and ECIS calculations. This work is supported by United States Department of Energy (USDOE) Contracts DE-AM03-76SF00326 (Stanford University), W-7405-ENG-48 Lawrence Livermore National Laboratory (LLNL), and DE-AC03-76SF00098 Lawrence Berkeley Laboratory (LBL). KVB gratefully acknowledges support from an A. P. Sloan Research Fellowship.

APPENDIX A: SUM RULES

The isoscalar transition operators for transitions of multipolarity λ are usually written as

$$O_{\lambda\mu} = \frac{Z}{A} \sum_k r_k^\lambda Y_{\lambda\mu}(\Omega_k), \quad (\text{A1})$$

where the index k runs over all of the nucleons in the nucleus. This expression holds for $\lambda \geq 2$. [The cases of $\lambda = 0$ and 1 (GMR and GDR) require special treatment.] If F is a Hermitian operator, and the nuclear Hamiltonian contains no velocity-dependent potential energy terms, then certain sum rules can be shown to hold, which limit the size of the matrix elements of the operator F :

$$\begin{aligned} S(F) &\equiv \sum_n (E_n - E_0) |\langle n|F|0\rangle|^2 \\ &= \frac{1}{2} \langle 0|[F, (H, F)]|0\rangle. \end{aligned} \quad (\text{A2})$$

When F is the multipole operator, the energy-weighted sum can be expressed in terms of radial moments of the ground-state nucleon density:

$$\begin{aligned} S(F) &= \sum_f (E_f - E_i) B(IS\lambda, J_i \rightarrow J_f) \\ &= \frac{2}{8M\pi} \lambda(2\lambda+1)^2 \frac{Z^2}{A} \langle r^{2\lambda-2} \rangle \quad (\lambda \geq 2), \end{aligned} \quad (\text{A3})$$

where

$$B(IS\lambda, J_i \rightarrow J_f) \equiv |\langle f||O_\lambda||i\rangle|^2.$$

This quantity is proportional to the cross section $d\sigma_{fi}/d\Omega$. The cross section per unit strength and the angular distribution of scattered particles are not very sensitive to the specific nuclear model used. Having measured a cross section for a transition of multipolarity λ , one uses a distorted-wave Born approximation (DWBA) or coupled-channels calculation to convert the cross section to multipole strength. The fraction of the energy-weighted sum rule exhausted by a transition is then a measure of its collectivity.

Table VI shows the isoscalar transition operators and

TABLE VI. Isoscalar operators and sum-rule values. $\lambda = 0, 1$ from Ref. 21.

λ	$O_{\lambda\mu}$	$S(IS\lambda)$
0	$(Z/A) \sum_k r_k^2$	$1.007 \times 10^5 \text{ MeV fm}^4$
1	$(Z/2A) \sum_k r_k^3 Y_{1\mu}(\Omega_k)$	$3.213 \times 10^5 \text{ MeV fm}^6$
2	$(Z/A) \sum_k r_k^2 Y_{2\mu}(\Omega_k)$	$1.002 \times 10^5 \text{ MeV fm}^4$

sum-rule values for the cases of $\lambda=0, 1$, and 2. The cases $\lambda=0$ and $\lambda=1$ are worked out by Harakeh and Dieperink²⁰ and are quoted in Table VI.

APPENDIX B: DWBA AND ECIS CALCULATIONS

In our calculations of the angular distribution, we used a vibrational-model transition density²¹ for the isoscalar quadrupole transition

$$\rho_{fi}^{(\lambda)}(r) = -\frac{\beta_\lambda R_0}{\sqrt{2\lambda+1}} \frac{\partial}{\partial r} \rho_0(r) \quad (\lambda \geq 2), \quad (\text{B1a})$$

and for the isoscalar monopole, we used²²

$$\rho_{fi}^{(0)}(r) = -\beta_0 \left[3 + r \frac{\partial}{\partial r} \right] \rho_0(r) \quad (\lambda=0), \quad (\text{B1b})$$

where $\rho_0(r)$ is the nucleon density of the ground state, and β_λ is the deformation parameter. The matrix elements of the isoscalar transition operators are then given by

$$M(IS\lambda) = \int \rho_{fi}^{(\lambda)}(r) r^{\lambda+2} dr \quad (\lambda \geq 2), \quad (\text{B2a})$$

$$M(IS0) = \int \rho_{fi}^{(0)}(r) r^4 dr \quad (\lambda=0). \quad (\text{B2b})$$

We assume that the optical potential is generated by folding a scalar potential $v(|\mathbf{r}-\mathbf{r}'|)$ with the ground-state nucleon density, and that the transition potential can be found by folding the same scalar potential with the transition density. Since the densities are real, it can be shown²³ (using a theorem due to Satchler) that

$$M(IS\lambda) = \frac{\int \text{Re} U_{fi}(r) r^{\lambda+2} dr}{\int \text{Re} U_{\text{opt}}(r) r^2 dr} = \frac{\int \text{Im} U_{fi}(r) r^{\lambda+2} dr}{\int \text{Im} U_{\text{opt}}(r) r^2 dr}. \quad (\text{B3})$$

(For the monopole, one sets $\lambda=2$ in the exponents.) Since the geometry of the optical potential is different for

the real and imaginary parts, different values of the coupling parameter β_λ must be used if (B3) is to be satisfied.

The program BEL (Ref. 23) was used to calculate β_R and β_I . BEL calculates the deformation parameters corresponding to full exhaustion of the energy-weighted sum rule, using (B3). It requires the optical and transition potentials as input. We used a Woods-Saxon form for the optical potential, with the parameters shown in Table III. (These parameters have been shown to give a good description of α scattering on ²⁰⁸Pb and ²³²Th.²⁴) The transition potentials used were

$$U_{fi}(r) \propto -R_0 \frac{\partial}{\partial r} U_{\text{opt}}(r) \quad (\lambda \geq 2), \quad (\text{B4a})$$

for the quadrupole, and for the monopole, the Satchler version I form factor:²²

$$U_{fi}(r) \propto - \left[3 + r \frac{\partial}{\partial r} \right] U_{\text{opt}}(r) \quad (\lambda=0), \quad (\text{B4b})$$

These were also the potentials which were used in the distorted-wave calculations.

The monopole angular distribution was calculated using DWUCK4, and the $\lambda=2$ distribution with the program ECIS79. The transition potential used by DWUCK was calculated for $\beta_R=1$, with the imaginary part scaled by the ratio β_I/β_R . To obtain the cross section for full exhaustion of the sum rule, the output was multiplied by β_R^2 . The program ECIS accepts the values of β_R , β_I , and β_C (the Coulomb deformation parameter) directly, so no renormalization of the cross section is necessary. Only the ground state (0^+) and the quadrupole state (2^+) were included in the ECIS calculation. ECIS was used because it handles the Coulomb excitation to the 2^+ state correctly. This makes a difference at forward scattering angles ($\theta'_\alpha < 10^\circ$). For $\theta'_\alpha > 10^\circ$, ECIS and DWUCK cross sections for the quadrupole were in close agreement.

*Present address: Vrije Universiteit Amsterdam, 1081 HV Amsterdam, The Netherlands.

†Present address: Department of Physics, University of Pennsylvania, Philadelphia, PA 19104.

‡Present address: Lawrence Livermore National Laboratory, Livermore, CA 94550.

¹J. van der Plicht, M. N. Harakeh, A. van der Woude, P. David, J. Debrus, H. Janszen, and J. Schulze, Nucl. Phys. **A346**, 49 (1980).

²F. E. Bertrand, J. R. Beene, C. E. Bemis, E. E. Gross, D. J. Horen, J. R. Wu, and W. P. Jones, Phys. Lett. **99B**, 213 (1981).

³S. Brandenburg, R. De Leo, A. G. Drentje, M. N. Harakeh, H. Janszen, and A. van der Woude, Phys. Rev. Lett. **49**, 1687 (1982); R. de Leo, S. Brandenburg, A. G. Drentje, M. N. Harakeh, H. Janszen, and A. van der Woude, Nucl. Phys. **A441**, 591 (1985).

⁴D. H. Dowell, L. S. Cardman, P. Axell, G. Bolme, and S. E. Williamson, Phys. Rev. Lett. **49**, 113 (1982).

⁵K. A. Griffioen, P. J. Countryman, K. T. Knöpfle, K. Van

Bibber, M. R. Yearian, J. G. Woodworth, D. Rowley, and J. R. Calarco, Phys. Rev. Lett. **53**, 2382 (1984); K. A. Griffioen, P. J. Countryman, K. T. Knöpfle, K. Van Bibber, M. R. Yearian, J. G. Woodworth, D. Rowley, and J. R. Calarco, Phys. Rev. C **34**, 1375 (1986).

⁶Th. Weber, R. D. Heil, U. Kneissl, W. Pecho, W. Wilke, H. J. Emrich, Th. Kihm, and K. T. Knöpfle, Phys. Rev. Lett. **59**, 2028 (1987).

⁷A. Veyssièrè, H. Beil, R. Bergère, P. Carlos, A. Lepretre, and K. Kernbath, Nucl. Phys. **A199**, 45 (1973).

⁸J. T. Caldwell, E. J. Dowdy, B. L. Berman, R. A. Alvarez, and P. Meyer, Phys. Rev. C **21**, 1215 (1980).

⁹Serious efforts have been made to extract resonances in the continuum by inclusive electron scattering. See, for example, R. Pitthan, F. R. Buskirk, W. A. Houk, and R. W. Moore, Phys. Rev. C **21**, 28 (1980) for ²³⁸U.

¹⁰D. Zawischa and J. Speth, in *Dynamics of Nuclear Fission and Related Collective Phenomena*, Vol. 158 of *Lecture Notes in Physics*, edited by P. David, T. Mayer-Kuckuk, and A. van der Woude (Springer-Verlag, Berlin, 1982), p. 231.

- ¹¹T. J. Deal and S. Fallieros, *Phys. Rev. C* **7**, 1709 (1973); J. V. Noble, *Ann. Phys.* **67**, 98 (1971).
- ¹²J. D. T. Arruda-Neto, R. Avida, J. R. Calarco, K. A. Griffioen, D. H. H. Hoffmann, K. T. Knöpfle, K. Van Bibber, R. Westervelt, and J. G. Woodworth, *Nucl. Instrum. Methods* **190**, 203 (1981).
- ¹³A. Koster, in *Prompt Fission Neutron Spectra* (IAEA, Vienna, 1972), p. 19.
- ¹⁴M. Drosch, *Nucl. Instrum. Methods* **105**, 573 (1972).
- ¹⁵Note that our R may be different—either smaller or greater—than Γ_n/Γ_f above $S_{2n} = 11.28$ MeV. Γ_n/Γ_f , in contrast, is determined only by the primary decay, n or f , of ^{238}U at E_x , and has nothing to do with the decay of subsequent daughters.
- ¹⁶P. D. Kunz, program DWUCK, University of Colorado (unpublished).
- ¹⁷J. Raynal, *Computing as a Language of Physics* (IAEA, Vienna, 1972), pp. 281–322.
- ¹⁸J. R. Calarco, Ph.D. thesis, University of Illinois, 1969.
- ¹⁹G. O. Bolme, L. S. Cardman, R. Doerfler, L. J. Koester, Jr., B. L. Miller, C. N. Papanicolas, H. Rothhaas, and S. E. Williamson [*Phys. Rev. Lett.* **61**, 1081 (1988)] have recently demonstrated the feasibility of neutron decay measurements in electron scattering ($e, e'n$).
- ²⁰M. N. Harakeh and A. E. L. Dieperink, *Phys. Rev. C* **23**, 2329 (1981).
- ²¹A. Bohr and B. Mottelson, *Nuclear Structure* (Benjamin, New York, 1969), Vol. I.
- ²²G. R. Satchler, *Part. Nucl.* **5**, 105 (1973).
- ²³M. N. Harakeh, Kernfysisch Versneller Instituut, Internal Report KVI-77i, 1981, and references therein.
- ²⁴M. N. Harakeh, B. van Heyst, K. van der Borg, and A. van der Woude, *Nucl. Phys.* **A327**, 373 (1979); M. N. Harakeh, K. van der Weg, A. van der Woude, H. P. Morsch, and F. E. Bertrand, *Phys. Rev. C* **21**, 768 (1980).